Rotational Slip Flow in Coaxial Cylinders by the Finite-Difference Lattice Boltzmann Methods

Minoru Watari*

LBM Fluid Dynamics Laboratory, 3-2-1 Mitahora-higashi, Gifu 502-0003, Japan.

Abstract. Recent studies on applications of the lattice Boltzmann method (LBM) and the finite-difference lattice Boltzmann method (FDLBM) to velocity slip simulations are mostly on one-dimensional (1D) problems such as a shear flow between parallel plates. Applications to a 2D problem may raise new issues. The author performed numerical simulations of rotational slip flow in coaxial cylinders as an example of 2D problem. Two types of 2D models were used. The first were multi-speed FDLBM models proposed by the author. The second was a standard LBM, the D2Q9 model. The simulations were performed applying a finite difference scheme to both the models. The study had two objectives. The first was to investigate the accuracies of LBM and FDLBM on applications to rotational slip flow. The second was to obtain an experience on application of the cylindrical coordinate system. The FDLBM model with 8 directions and the D2Q9 model showed an anisotropic flow pattern when the relaxation time constant or the Knudsen number was large. The FDLBM model with 24 directions showed accurate results even at large Knudsen numbers.

PACS: 47.11.-j, 47.45.-n, 51.10.+y

Key words: Finite-difference lattice Boltzmann method, rarefied gas flow, rotational slip flow, cylindrical coordinate.

1 Introduction

A rarefied gas flow is represented properly by the Boltzmann equation. However, the Boltzmann equation is an equation in the phase space: physical space plus velocity space. Burden in computing is enormous. Therefore, in an intermediate flow such as the velocity slip, where both the Navier-Stokes flow and the rarefied gas flow co-exist, the lattice Boltzmann method (LBM) and the finite-difference lattice Boltzmann method (FDLBM) are potentially ideal flow solvers if they can represent the rarefied gas flow properly.

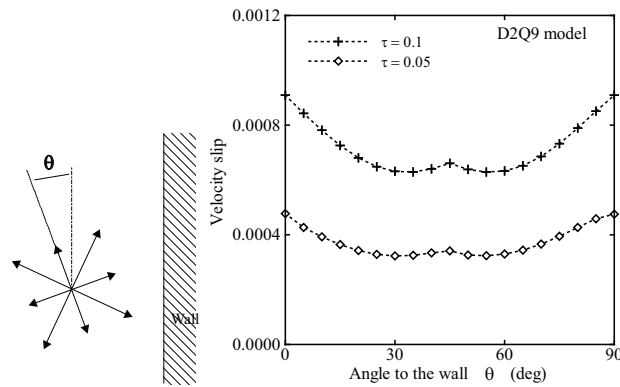*Corresponding author. *Email address:* `watari-minoru@kvd.biglobe.ne.jp` (M. Watari)

Figure 1: Velocity slip fluctuations by the relative angle to the wall.

There are many recent studies on applications of the LBM and the FDLBM to velocity slip simulations [1–10]. Most studies so far are applications to one-dimensional (1D) problems such as a shear flow between parallel plates. The author conducted a simulation of shear flow between parallel plates using the D2Q9 model [11] and found that the velocity slip fluctuates considerably (32 percents) when the relative angle to the wall changes (see Fig. 1). Therefore, in order to apply the LBM or FDLBM to 2D problems, the dependency on the inclination angle must be decreased by increasing the number of directions of velocity particles.

In this study, the author studied a 2D problem, simulating a rotational slip flow. Two types of 2D models were used. The first are multi-speed thermal FDLBM [12] and its derivative models with different number of velocity particles. The second is the standard LBM model, D2Q9 [13]. The cylindrical coordinate system was adopted in the simulation. To obtain an experience on application of the cylindrical coordinate system to a slip flow is another objective of this study. Before proceeding to the FDLBM simulations, a review of a no-slip solution by the Navier-Stokes analysis and numerical simulations by the continuous Boltzmann equation were conducted to understand the rotational slip phenomena.

Quantities used in this paper are nondimensional based on the reference density ρ_0, the reference length L, and the reference temperature T_0 (where R is gas constant).

Length (x,y,r)	by	L,
Speed $(u_r, u_\theta, c, c_k, c_{ki\alpha})$	by	$\sqrt{RT_0}$,
Time (t, τ)	by	$L/\sqrt{RT_0}$,
Internal energy (e)	by	RT_0,
Density, distribution function $(\rho, f_{ki}, f_{ki}^{eq})$	by	ρ_0,
Distribution function per unit velocity volume (f, f^{eq})	by	$\rho_0/(RT_0)$,
Momentum flow $(P_{\theta r})$	by	$\rho_0 RT_0$,

Torque (T, T_{intg})	by	$\rho_0 R T_0 L^2$,
Viscosity (μ)	by	$\rho_0 \sqrt{R T_0} L$,
Angle (θ, ϕ)	by	rad,
Angular velocity (ω)	by	$\text{rad}\sqrt{R T_0}/L$.

2 Analytical solution by the Navier-Stokes equations

Schematic view of the rotational slip flow is shown in Fig. 2. Gas is filled between coaxial cylinders, whose radii are $r_1 = 1.0$ and $r_2 = 2.0$. The inner cylinder is at rest while the outer cylinder rotates at constant speed $u_{\theta w} = 0.01$.
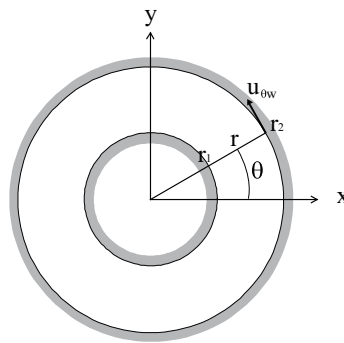

Figure 2: Schematic view of rotational slip flow.

Analytical solution based on the Navier-Stokes equations is presented as follows [14]. The torque T per unit angle acting on the layer of gas at radius r is

$$T = \mu r^3 \frac{d\omega}{dr}, \tag{2.1}$$

where μ is the viscosity coefficient and ω is the angular velocity. Therefore, the torque T_{intg} integrated over the angle $\theta = 0$ to 2π is

$$T_{intg} = \int_0^{2\pi} T d\theta = 2\pi \mu r^3 \frac{d\omega}{dr}. \tag{2.2}$$

The differential equation (2.2) is readily integrated since in a steady state T_{intg} is not dependent on r,

$$T_{intg} \int_{r_1}^{r_2} \frac{dr}{r^3} = 2\pi \mu \int_{\omega_1}^{\omega_2} d\omega. \tag{2.3}$$

Therefore, since $\omega_1 = 0.0$ and $\omega_2 = u_{\theta w}/r_2$, the following torque formula for no-slip Navier Stokes solution is obtained:

$$T_{intg} = 4\pi \mu \frac{r_1^2 r_2^2}{r_2^2 - r_1^2} \frac{u_{\theta w}}{r_2}. \tag{2.4}$$

The angular velocity ω and the rotational velocity u_θ at radius r are expressed as follows:

$$\omega = \frac{T_{intg}}{4\pi\mu}\left(\frac{1}{r_1^2} - \frac{1}{r^2}\right), \qquad u_\theta = \frac{T_{intg}}{4\pi\mu}\left(\frac{1}{r_1^2} - \frac{1}{r^2}\right)r. \tag{2.5}$$

3 Solution by the continuous Boltzmann equation

The rotational slip flow was solved by the continuous Boltzmann equation applying the diffuse reflection condition to the walls. The cylindrical coordinate system, the physical space (r,θ) and the velocity space (c,ϕ) shown in Fig. 3, was applied.
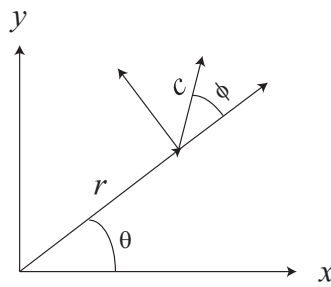

Figure 3: Cylindrical coordinate system used in the continuous Boltzmann simulation.

The Boltzmann equation for the distribution function f with the BGK collision term (relaxation time constant τ) is written as (see Appendix)

$$\frac{\partial f}{\partial t} + c\cos\phi\frac{\partial f}{\partial r} + \frac{c\sin\phi}{r}\left(\frac{\partial f}{\partial \theta} - \frac{\partial f}{\partial \phi}\right) = -\frac{f - f^{eq}}{\tau}, \tag{3.1a}$$

$$f^{eq} = \frac{\rho}{2\pi e}\exp\left[-\frac{c^2 + u_r^2 + u_\theta^2 - 2c(u_r\cos\phi + u_\theta\sin\phi)}{2e}\right]. \tag{3.1b}$$

Sufficiently fine grid system was applied to obtain accurate data for comparison with the FDLBM simulations, which enabled us to drop the angle θ from the independent variables in view of the cylindrical symmetry ($\partial/\partial\theta = 0$).

The macroscopic quantities of the density ρ, the radial velocity u_r, the rotational velocity u_θ, and the internal energy e are obtained integrating the following moments of the distribution function, where $d\mathbf{c}$ is a volume element in the velocity space ($d\mathbf{c} = cdcd\phi$):

$$\rho = \int fd\mathbf{c}, \tag{3.2a}$$

$$\rho u_r = \int fc\cos\phi d\mathbf{c}, \qquad \rho u_\theta = \int fc\sin\phi d\mathbf{c}, \tag{3.2b}$$

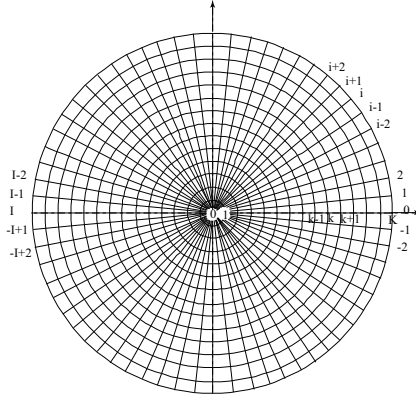$$\rho\left(e + \frac{u^2}{2}\right) = \int f\frac{c^2}{2}d\mathbf{c}. \tag{3.2c}$$

Figure 4: Grid of the velocity space used in the continuous Boltzmann simulation.

The viscosity coefficient μ has the following relationship:

$$\mu = \rho e \tau. \tag{3.3}$$

The radial position and the velocity space were discretized as follows (see Fig. 4):

$$r = r_1 + n\Delta r \quad (n = 0, \cdots, N), \tag{3.4a}$$

$$c = k\Delta c \quad\quad (k = 0, \cdots, K), \tag{3.4b}$$

$$\phi = i\Delta\phi \quad\quad (i = -I+1, \cdots, 0, \cdots, I), \tag{3.4c}$$

where the increments are as follows (c_{co} is a cut off speed):

$$\Delta r = \frac{r_2 - r_1}{N}, \qquad \Delta c = \frac{c_{co}}{K}, \qquad \Delta\phi = \frac{\pi}{I}. \tag{3.5}$$

In the gas region $r_1 < r < r_2$ (or $1 \leq n \leq N-1$), the distribution function f^{new} at $t+\Delta t$ was calculated from the distribution $f(r,c,\phi)$ (or $f(n,k,i)$ by the grid expression) at t by the following finite difference scheme:

$$f^{new} = f - \left[c\cos\phi \frac{\partial f}{\partial r} - \frac{c\sin\phi}{r} \frac{\partial f}{\partial \phi} + \frac{f - f^{eq}}{\tau} \right] \Delta t. \tag{3.6}$$

The derivatives were calculated by the second order upwind scheme as follows, where the only variable pertinent to the differentiation is indicated as the subscript:

$$\frac{\partial f}{\partial r} = \begin{cases} \dfrac{3f_n - 4f_{n-1} + f_{n-2}}{2\Delta r}, & \text{if } \cos\phi \geq 0, \\[2mm] \dfrac{3f_n - 4f_{n+1} + f_{n+2}}{-2\Delta r}, & \text{if } \cos\phi < 0, \end{cases} \tag{3.7a}$$

$$\frac{\partial f}{\partial \phi} = \begin{cases} \dfrac{3f_i - 4f_{i-1} + f_{i-2}}{2\Delta\phi}, & \text{if } \sin\phi < 0, \\[2mm] \dfrac{3f_i - 4f_{i+1} + f_{i+2}}{-2\Delta\phi}, & \text{if } \sin\phi \geq 0. \end{cases} \tag{3.7b}$$

However, at the node $n=1$, for $\cos\phi \geq 0$, and at the node $n=N-1$, for $\cos\phi < 0$, the second order upwind scheme (3.7a) is not applicable. The first order upwind scheme was applied there,

$$\frac{\partial f}{\partial r}\Big|_{n=1}=\frac{f_1-f_0}{\Delta r} \quad (\cos\phi\geq 0), \qquad \frac{\partial f}{\partial r}\Big|_{n=N-1}=\frac{f_{N-1}-f_N}{-\Delta r} \quad (\cos\phi<0). \tag{3.8}$$

The boundary condition on the outer cylinder $(n=N)$ is as follows.

The incident distribution f_N $(\cos\phi \geq 0)$ was calculated from the gas region by the evolution equation (3.6) with the second order upwind scheme (3.7a) and (3.7b). The emissive distribution $(\cos\phi < 0)$ is a local equilibrium distribution $f^{eq}(\rho_w, u_{\theta w}, e_w)$. The density ρ_w is determined so as to give a zero mass flow normal to the wall,

$$\int_{\cos\phi>0}f_N c\cos\phi d\mathbf{c}+\int_{\cos\phi<0}f^{eq}(\rho_w,u_{\theta w},e_w)c\cos\phi d\mathbf{c}=0. \tag{3.9}$$

Consequently, the density ρ_w was calculated as

$$\rho_w=-\frac{\int_{\cos\phi>0}f_N c\cos\phi d\mathbf{c}}{\int_{\cos\phi<0}f^{eq}(\rho_w=1.0,u_{\theta w},e_w)c\cos\phi d\mathbf{c}}. \tag{3.10}$$

The boundary condition on the inner cylinder $(n=0)$ was performed in a similar way.

The integrations (3.2a)-(3.2c) and (3.10) were calculated by the trapezoidal rule. For example, $\int f d\mathbf{c}$ was calculated as follows, where $f(n,k,i)$ is abbreviated to $f_{k,i}$:

$$\int f d\mathbf{c}=\Delta\phi\Delta c^2\Bigg[\frac{I}{3}f_{0,0}+\sum_{i=-I+1}^{I}f_{1,i}+2\sum_{i=-I+1}^{I}f_{2,i}+\cdots$$
$$+(K-1)\sum_{i=-I+1}^{I}f_{K-1,i}+\frac{3K-1}{6}\sum_{i=-I+1}^{I}f_{K,i}\Bigg]. \tag{3.11}$$

The number of radial grids N and the number of azimuthal grids I in the velocity space were set as the same values of radial grids N and azimuthal grids J in the physical space for the FDLBM simulation, which will be shown in the next section.

$$N=100 \quad (\Delta r=0.01), \qquad I=100 \quad (\Delta\phi=0.01\pi). \tag{3.12}$$

Dependence study for the number of velocity speed grids K was performed with the cut-off speed $c_{co}=6.0$. The grid Δc has an effect on the accuracy through the integrations (3.2a)-(3.2c) and (3.10). It was investigated whether Eqs. (3.2a)-(3.2c) reproduce accurate macroscopic quantities when the equilibrium distribution f^{eq} ($\rho=1.0$, $u_r=0.0$, $u_\theta=0.01$, $e=1.0$) is substituted to the equations. The relative errors $(u_\theta-0.01)/0.01$, for $K=100,200,400,600,800,1000$ with $I=100$ are shown in Fig. 5. The convergence rate is second order as Eq. (3.11) implies. The value of K was determined so that the relative
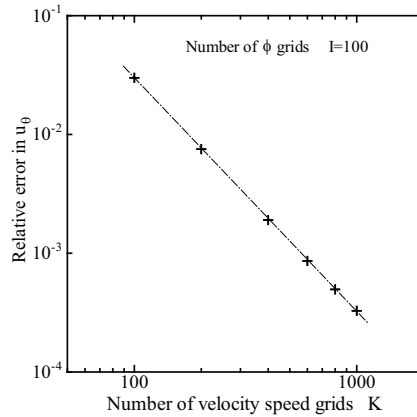
Figure 5: Dependence study for the number of velocity speed grids K.

error is an order of 0.1 % (or 10^{-3}). Consequently, following values were applied to the simulation.

$$K = 500, \qquad c_{co} = 6.0, \qquad (\Delta c = 0.012). \tag{3.13}$$

Simulations for $\tau = 0.01, 0.05, 0.1, 0.2$ started from an equilibrium state at rest with $\rho = 1.0$ and $e = 1.0$. Time increment $\Delta t = 0.0008$ was commonly used in the continuous Boltzmann simulations.

The simulation result of the radial velocity u_r was zero at any radial position. The results of u_θ and ω versus r are shown in Fig. 6. The Boltzmann solution approaches the no-slip Navier-Stokes solution as expected as τ approaches zero.

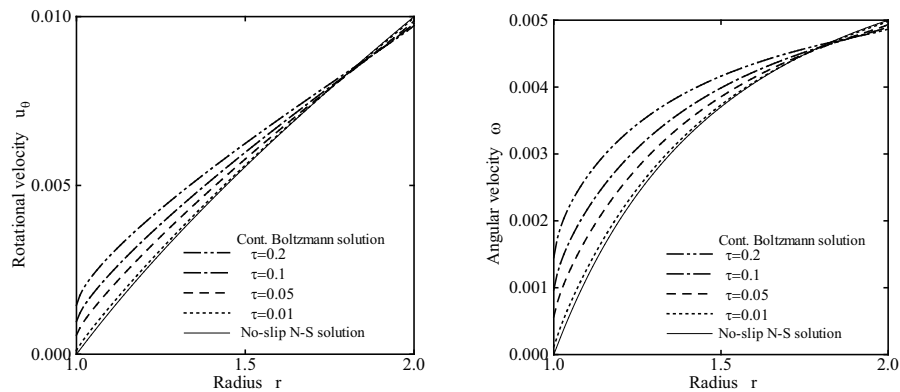Figure 6: Rotational velocity u_θ and angular velocity ω versus r by the continuous Boltzmann equation.

On the kinetic theory, the viscous force per unit area is defined by the momentum flow $P_{\theta r}$; consequently, the torque T per unit angle is defined as follows:

$$P_{\theta r} = \int f c_\theta c_r d\mathbf{c}, \qquad T = -r^2 P_{\theta r}, \tag{3.14}$$
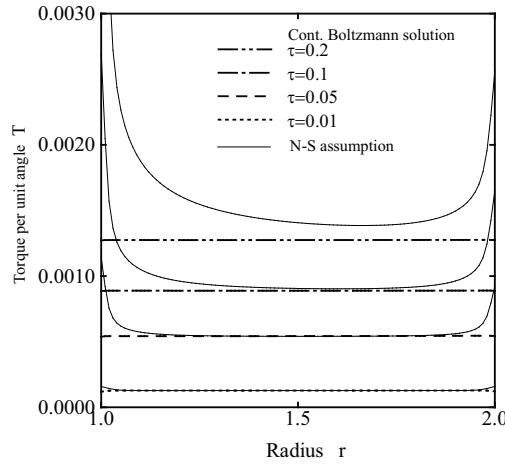
Figure 7: Torque T per unit angle for various τ by the continuous Boltzmann equation. The torque on the Navier-Stokes assumption for each τ is also shown to demonstrate the N-S flow area.

where $c_r = c\cos\phi$, and $c_\theta = c\sin\phi$.

The torque per unit angle calculated from the continuous Boltzmann simulation is shown in Fig. 7. It is constant through the area as the conservation law predicts. The torque per unit angle on the Navier-Stokes assumption (2.1) was calculated using ω by the continuous Boltzmann solution. It is shown in the same figure. The region where the Navier-Stokes assumption agrees with the $P_{\theta r}$ definition indicates the area where the Navier-Stokes equation is valid (N-S flow area). The figure shows that the N-S flow area dominates almost an entire region when $\tau = 0.01$. The N-S flow area shrinks as τ increases and when $\tau = 0.2$ the Navier-Stokes assumption is not valid anywhere.

4　Numerical simulations by the FDLBM models

4.1　Octagon family

Three models with different number of velocity particles were used: Octagon model, Double Octagon model and Triple Octagon model. Derivation of the models is presented in [11].

The evolution of the distribution function f_{ki} is governed by the following equations:

$$\frac{\partial f_{ki}}{\partial t} + c_{kix}\frac{\partial f_{ki}}{\partial x} + c_{kiy}\frac{\partial f_{ki}}{\partial y} = -\frac{1}{\tau}(f_{ki} - f_{ki}^{eq}), \tag{4.1a}$$

$$f_{ki}^{eq} = \rho F_k \left[\left(1 - \frac{u^2}{2e} + \frac{u^4}{8e^2}\right) + \frac{1}{e}\left(1 - \frac{u^2}{2e}\right)c_{ki\xi}u_\xi + \frac{1}{2e^2}\left(1 - \frac{u^2}{2e}\right)c_{ki\xi}c_{ki\eta}u_\xi u_\eta \right.$$
$$\left. + \frac{1}{6e^3}c_{ki\xi}c_{ki\eta}c_{ki\zeta}u_\xi u_\eta u_\zeta + \frac{1}{24e^4}c_{ki\xi}c_{ki\eta}c_{ki\zeta}c_{ki\chi}u_\xi u_\eta u_\zeta u_\chi \right]. \tag{4.1b}$$
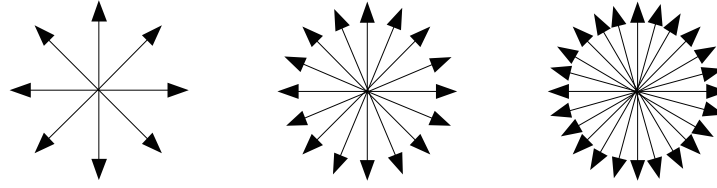
Figure 8: Unit vectors of moving particles of the Octagon family. From left to right, Octagon model, Double Octagon model, and Triple Octagon model.

Velocity particles of the models consist of a rest particle and 4 speeds of moving particles that go forward in 8, 16, and 24 directions. The moving particles (c_{kix}, c_{kiy}) for each model are obtained through multiplying the unit vectors (Fig. 8) by the speeds c_k ($k=1,2,3,4$).

For the Octagon model,

$$c_k\left(\cos\frac{2\pi}{8}(i-1), \sin\frac{2\pi}{8}(i-1)\right) \quad (i=1-8), \tag{4.2}$$

for the Double Octagon model,

$$c_k\left(\cos\frac{2\pi}{16}(i-1), \sin\frac{2\pi}{16}(i-1)\right) \quad (i=1-16), \tag{4.3}$$

and for the Triple Octagon model,

$$c_k\left(\cos\frac{2\pi}{24}(i-1), \sin\frac{2\pi}{24}(i-1)\right) \quad (i=1-24). \tag{4.4}$$

The macroscopic quantities of the density ρ, the velocity u_α, and the internal energy e are calculated from the distribution function,

$$\rho=\sum_{k,i} f_{ki}, \tag{4.5a}$$

$$\rho u_\alpha=\sum_{k,i} f_{ki} c_{ki\alpha}, \tag{4.5b}$$

$$\rho\left(e+\frac{u^2}{2}\right)=\sum_{k,i} f_{ki}\frac{c_k^2}{2}. \tag{4.5c}$$

The viscosity coefficient μ has the following relationship:

$$\mu=\rho e\tau. \tag{4.6}$$

The weighting coefficients F_k in the local equilibrium distribution function (4.1b) are

$$F_0=1-B_0(F_1+F_2+F_3+F_4), \tag{4.7a}$$

$$F_1 = \frac{B_4 e^4 + B_3(c_2^2 + c_3^2 + c_4^2)e^3 + B_2(c_2^2 c_3^2 + c_3^2 c_4^2 + c_4^2 c_2^2)e^2 + B_1 c_2^2 c_3^2 c_4^2 e}{c_1^2(c_1^2 - c_2^2)(c_1^2 - c_3^2)(c_1^2 - c_4^2)}, \qquad (4.7b)$$

$$F_2 = \frac{B_4 e^4 + B_3(c_3^2 + c_4^2 + c_1^2)e^3 + B_2(c_3^2 c_4^2 + c_4^2 c_1^2 + c_1^2 c_3^2)e^2 + B_1 c_3^2 c_4^2 c_1^2 e}{c_2^2(c_2^2 - c_3^2)(c_2^2 - c_4^2)(c_2^2 - c_1^2)}, \qquad (4.7c)$$

$$F_3 = \frac{B_4 e^4 + B_3(c_4^2 + c_1^2 + c_2^2)e^3 + B_2(c_4^2 c_1^2 + c_1^2 c_2^2 + c_2^2 c_4^2)e^2 + B_1 c_4^2 c_1^2 c_2^2 e}{c_3^2(c_3^2 - c_4^2)(c_3^2 - c_1^2)(c_3^2 - c_2^2)}, \qquad (4.7d)$$

$$F_4 = \frac{B_4 e^4 + B_3(c_1^2 + c_2^2 + c_3^2)e^3 + B_2(c_1^2 c_2^2 + c_2^2 c_3^2 + c_3^2 c_1^2)e^2 + B_1 c_1^2 c_2^2 c_3^2 e}{c_4^2(c_4^2 - c_1^2)(c_4^2 - c_2^2)(c_4^2 - c_3^2)}. \qquad (4.7e)$$

The coefficients B_0, B_4, B_3, B_2, and B_1 for each model are summarized in Table 1.

Table 1: Coefficients B_0, B_4, B_3, B_2, and B_1 for each model.

	B_0	B_4	B_3	B_2	B_1
Octagon	8	48	-6	1	-1/4
Double Octagon	16	24	-3	1/2	-1/8
Triple Octagon	24	16	-2	1/3	-1/12

Selection of the moving particle speeds c_k is arbitrary as far as the condition $0 < c_1 < c_2 < c_3 < c_4$ is satisfied. The speeds were determined so that the average particle speed agrees with the theoretical value, since in the BGK approximation, the Knudsen number Kn is defined by the relaxation time constant τ and the average particle speed $\bar{c}$,

$$Kn = \tau \bar{c}. \qquad (4.8)$$

The theoretical average particle speed is

$$\bar{c} = \sqrt{\frac{\pi}{2}} e. \qquad (4.9)$$

The FDLBM average particle speed was calculated using the equilibrium distribution with $u_\alpha = 0.0$,

$$\rho \bar{c} = \sum_{k,i} f_{ki}^{eq} c_k. \qquad (4.10)$$

The speeds were determined to give the best match around $e = 1.0$. Refer to [10] for the determination procedure. The result is $(c_1, c_2, c_3, c_4) = (0.816, 1.806, 2.978, 4.469)$, which is common to all three models. The average particle speed, which is common to all three models, is compared with the theory in Fig. 9.
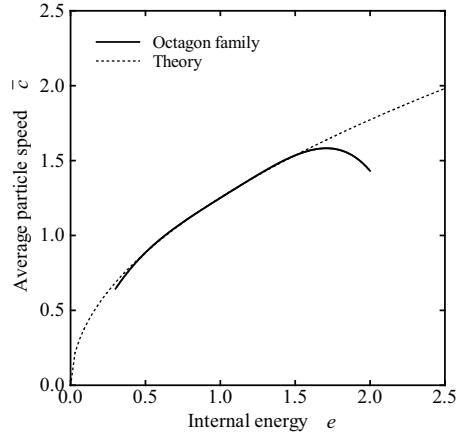
Figure 9: Average particle speed of the Octagon family and the theory.

4.2 D2Q9 model

The evolution of the distribution function f_i is governed by the following equations:

$$\frac{\partial f_i}{\partial t} + c_{ix}\frac{\partial f_i}{\partial x} + c_{iy}\frac{\partial f_i}{\partial y} = -\frac{1}{\tau}(f_i - f_i^{eq}), \tag{4.11a}$$

$$f_i^{eq} = \rho w_i\left[1 + 3\frac{c_{i\xi}u_\xi}{c^2} + \frac{9}{2}\frac{c_{i\xi}c_{i\eta}u_\xi u_\eta}{c^4} - \frac{3}{2}\frac{u^2}{c^2}\right]. \tag{4.11b}$$

The velocity particles (c_{ix}, c_{iy}) consist of a rest particle and 8 moving particles (Fig. 10),

$$(0,0) \qquad\qquad\qquad\qquad\qquad\qquad (i=0), \tag{4.12a}$$

$$c\left(\cos\left[\frac{\pi}{2}(i-1)\right], \sin\left[\frac{\pi}{2}(i-1)\right]\right) \qquad\qquad (i=1-4), \tag{4.12b}$$

$$\sqrt{2}c\left(\cos\left[\frac{\pi}{2}(i-5)+\frac{\pi}{4}\right], \sin\left[\frac{\pi}{2}(i-5)+\frac{\pi}{4}\right]\right) \quad (i=5-8), \tag{4.12c}$$

where c is the basic particle speed. In the simulation, $c=1.0$ was assumed.
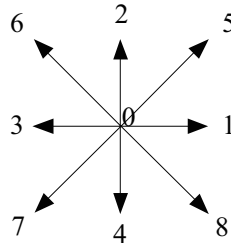

Figure 10: D2Q9 model particles.

The weighting coefficients w_i in the local equilibrium distribution function (4.11b) are defined as follows:

$$w_i = \frac{4}{9} \quad (i=0), \qquad \frac{1}{9} \quad (i=1-4), \qquad \frac{1}{36} \quad (i=5-8). \tag{4.13}$$

The macroscopic quantities of the density ρ and the velocity u_α are calculated from the distribution function,

$$\rho = \sum_i f_i, \tag{4.14a}$$

$$\rho u_\alpha = \sum_i f_i c_{i\alpha}. \tag{4.14b}$$

The viscosity coefficient μ has the following relationship:

$$\mu = \frac{1}{3}\rho c^2 \tau. \tag{4.15}$$

4.3   Numerical simulation scheme

The same finite-difference scheme was applied to the Octagon family and D2Q9 simulations. Since the difference between them is only in the subscript: ki versus i, in this section the formulation for the Octagon family is described.
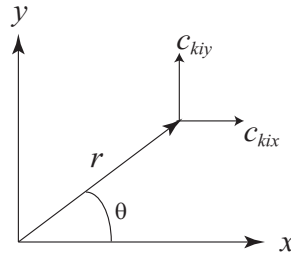

Figure 11: Cylindrical coordinate system used in the FDLBM simulation.

The cylindrical coordinate system was adopted to the physical space as shown in Fig. 11. Since the objective of the FDLBM simulation is to investigate the effect of the angle θ, the physical space shown in Fig. 12 was applied, different from the physical space of the continuous Boltzmann simulation in Section 3 where the cylindrical symmetry was used.

The position (r,θ) is expressed as the grid system (n,j),

$$r = r_1 + n\Delta r \quad (n=0,\cdots,N), \qquad \theta = j\Delta\theta \quad (j=-2,\cdots,J+2), \tag{4.16}$$

where the increments are defined as follows:

$$\Delta r = \frac{r_2 - r_1}{N}, \qquad \Delta\theta = \frac{\pi}{J}. \tag{4.17}$$
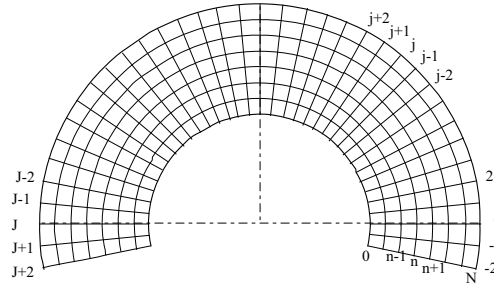
Figure 12: Grid of the physical space used in the FDLBM simulation.

In the gas region $r_1 < r < r_2$ (or $1 \leq n \leq N-1$), and $0 \leq \theta \leq \pi$ (or $0 \leq j \leq J$), the distribution function f_{ki}^{new} at $t + \Delta t$ was calculated from the distribution f_{ki} at t by the following finite difference scheme (see Appendix):

$$f_{ki}^{new} = f_{ki} - \left[c_{kir} \frac{\partial f_{ki}}{\partial r} + c_{ki\theta} \frac{\partial f_{ki}}{r \partial \theta} + \frac{1}{\tau} (f_{ki} - f_{ki}^{eq}) \right] \Delta t. \tag{4.18}$$

Velocities in the cylindrical coordinate have following relationships with those in the Cartesian coordinate:

$$c_{kir} = c_{kix} \cos\theta + c_{kiy} \sin\theta, \qquad c_{ki\theta} = -c_{kix} \sin\theta + c_{kiy} \cos\theta, \tag{4.19a}$$

$$u_r = u_x \cos\theta + u_y \sin\theta, \qquad u_\theta = -u_x \sin\theta + u_y \cos\theta. \tag{4.19b}$$

The derivatives at position (n, j) were calculated by the second order upwind scheme,

$$\frac{\partial f_{ki}}{\partial r} = \begin{cases} \dfrac{3 f_{ki,n} - 4 f_{ki,n-1} + f_{ki,n-2}}{2 \Delta r}, & \text{if } c_{kir} \geq 0, \\[2mm] \dfrac{3 f_{ki,n} - 4 f_{ki,n+1} + f_{ki,n+2}}{-2 \Delta r}, & \text{if } c_{kir} < 0, \end{cases} \tag{4.20a}$$

$$\frac{\partial f_{ki}}{\partial \theta} = \begin{cases} \dfrac{3 f_{ki,j} - 4 f_{ki,j-1} + f_{ki,j-2}}{2 \Delta \theta}, & \text{if } c_{ki\theta} \geq 0, \\[2mm] \dfrac{3 f_{ki,j} - 4 f_{ki,j+1} + f_{ki,j+2}}{-2 \Delta \theta}, & \text{if } c_{ki\theta} < 0. \end{cases} \tag{4.20b}$$

However, at the node $n = 1$, for $c_{kir} \geq 0$, and at the node $n = N-1$, for $c_{kir} < 0$, the second order upwind scheme (4.20a) is not applicable. The first order upwind scheme was applied there,

$$\frac{\partial f_{ki}}{\partial r} \bigg|_{n=1} = \frac{f_{ki,1} - f_{ki,0}}{\Delta r} \quad (c_{kir} \geq 0), \qquad \frac{\partial f_{ki}}{\partial r} \bigg|_{n=N-1} = \frac{f_{ki,N-1} - f_{ki,N}}{-\Delta r} \quad (c_{kir} < 0). \tag{4.21}$$

The boundary condition on the outer cylinder $(n = N)$ is as follows. The incident distribution $f_{ki,N}$ $(c_{kir} \geq 0)$ was calculated from the gas region by the evolution equation (4.18) with the second order upwind scheme (4.20a) and (4.20b).

The emissive distribution $(c_{kir} < 0)$ is a local equilibrium distribution $f_{ki}^{eq}(\rho_w, u_{\theta w}, e_w)$. The density ρ_w was determined so as to give a zero mass flow normal to the wall,

$$\rho_w = -\frac{\sum_{c_{kir} > 0} f_{ki,N} c_{kir}}{\sum_{c_{kir} < 0} f_{ki}^{eq}(\rho_w = 1.0, u_{\theta w}, e_w) c_{kir}}. \tag{4.22}$$

The boundary condition on the inner cylinder $(n = 0)$ was treated in a similar way.

To ensure the second order upwind scheme for $\partial f_{ki} / \partial \theta$ (4.20b) at $\theta = 0$ and π, two lines of extra grids, $j = -1, -2$, and $j = J+1, J+2$, were added at each end. The distributions $f_{ki,j}$ at the extra grids were given utilizing anti-symmetrical relationship as follows:

$$f_{0,-1} = f_{0,J-1}, \quad f_{0,-2} = f_{0,J-2}, \qquad f_{ki,-1} = f_{ki^\star, J-1}, \quad f_{ki,-2} = f_{ki^\star, J-2}, \tag{4.23a}$$

$$f_{0,J+1} = f_{0,1}, \quad f_{0,J+2} = f_{0,2}, \qquad f_{ki,J+1} = f_{ki^\star, 1}, \quad f_{ki,J+2} = f_{ki^\star, 2}, \tag{4.23b}$$

where the subscript $i^\star$ indicates the opposite direction of the subscript i. As an example, the anti-symmetrical relation for the Octagon model is shown in Table 2.

Table 2: Anti-symmetrical relation for the Octagon model.

i	1	2	3	4	5	6	7	8
$i^\star$	5	6	7	8	1	2	3	4

Grid dependence study was performed using the Octagon model with $\tau = 0.2$ varying the number of radial grids N and the number of azimuthal grids J. The effect of N was investigated varying $N = 25, 50, 100, 150$ with $J = 100$. Assuming the finest case is the true solution, following RMS error was evaluated at the common 26 radial positions.

$$\Delta u_\theta = \sqrt{\frac{\sum (u_\theta - u_{\theta.true})^2}{\text{number of samples}}}. \tag{4.24}$$

Similarly the effect of J was investigated varying $J = 30, 50, 100, 150$, with $N = 100$. The relative errors $\Delta u_\theta / u_{\theta w}$ are shown in Fig. 13. The values of N and J were determined so that the relative error is less than 0.1 % (or 10^{-3}). $N = 50$ is satisfactory. However, following values were applied to the simulation:

$$N = 100 \quad (\Delta r = 0.01), \qquad J = 100 \quad (\Delta \theta = 0.01\pi). \tag{4.25}$$

Time increment $\Delta t = 0.001$ was commonly used in the FDLBM simulations.

5   Results of the FDLBM simulation

5.1   Results by the Octagon family

Simulations for $\tau = 0.01, 0.05, 0.1$, and 0.2 started from an equilibrium state at rest with $\rho = 1.0$ and $e = 1.0$. The steady state rotational velocity u_θ in the flow domain for the
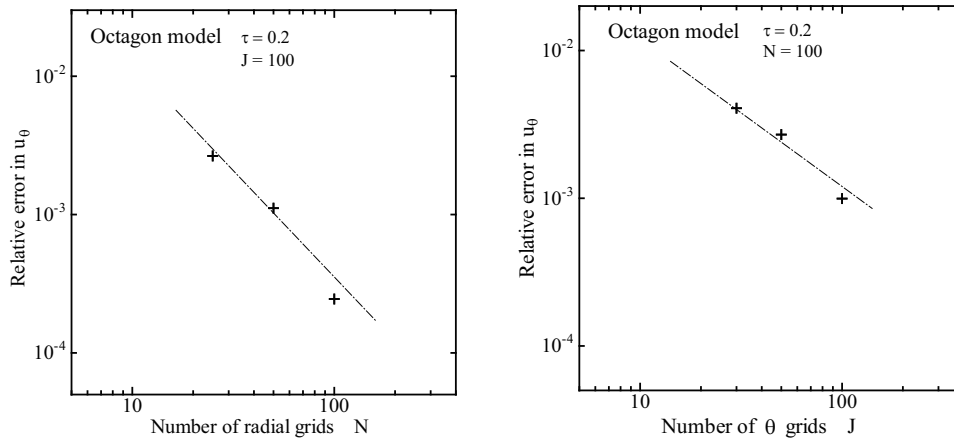
Figure 13: Dependence study for the number of radial grids N and the number of azimuthal grids J.
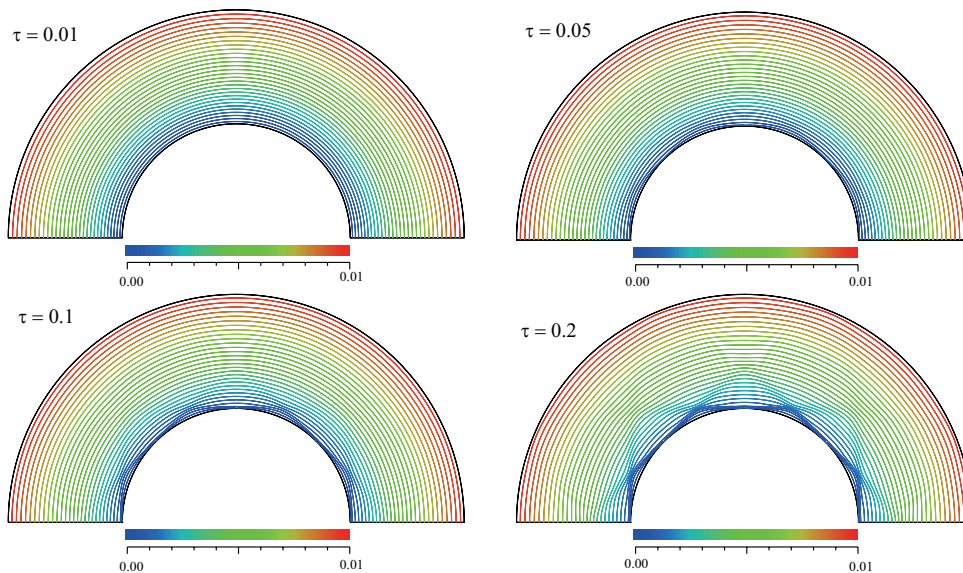

Figure 14: Octagon model. Rotational velocity u_θ in the flow domain for $\tau = 0.01, 0.05, 0.1$ and 0.2.

Octagon model with various τ are shown in Fig. 14. The flow is uniform for small τ, however, non-uniformity becomes prominent as τ increases.

To confirm it more clearly, the rotational velocity u_θ for $\tau = 0.2$ at the angles $\theta = 0, \pi/10, \pi/5$ (or $0°, 18°, 36°$) are shown in Fig. 15. The model's dependence on the angle θ, in particular in the vicinity of the inner cylinder, is apparent. The u_θ distributions for the Double Octagon and the Triple Octagon are shown in Fig. 16. For the Triple Octagon model, the dependence is almost negligible and the agreement with the continuous Boltzmann solution is perfect.
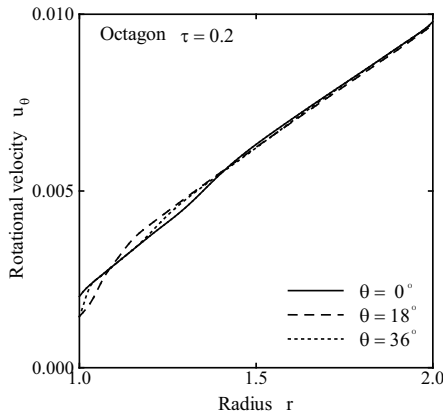
Figure 15: Rotational velocity u_θ versus r for Octagon model with $\tau=0.2$ at $\theta=0°,18°,36°$.
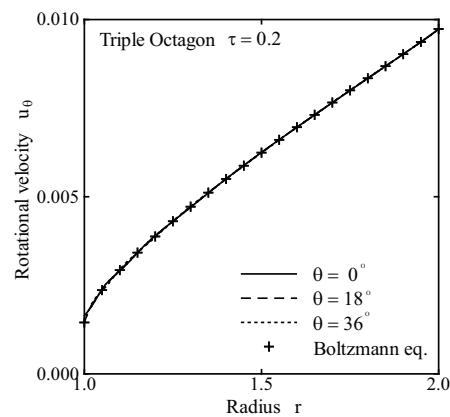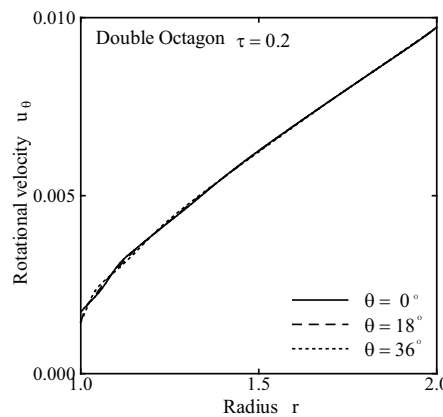

Figure 16: Rotational velocity u_θ versus r for Double Octagon and Triple Octagon model with $\tau=0.2$ at $\theta=0°,18°,36°$. For Triple Octagon model, simulation result by the continuous Boltzmann equation is shown for comparison.

The torque T per unit angle was calculated as

$$T=-r^2 P_{\theta r}=-r^2\sum_{k,i}f_{ki}c_{ki\theta}c_{kir}. \tag{5.1}$$

The torque per unit angle at the angles $\theta=0°,18°,36°$ for the Octagon, Double Octagon, and Triple Octagon are shown in Fig. 17. The torque T_{av} averaged over $\theta=0$ to π are also shown in the figures. Although the torque T at each θ fluctuates, the average T_{av} is constant.

The torque T_{intg} was obtained by multiplying T_{av} at $r=1.5$ by 2π. The difference of T_{intg} between the Octagon, Double Octagon, and Triple Octagon is very small. T_{intg} for the Triple Octagon versus τ is shown in Fig. 18. The no-slip solution by the Navier-Stokes equation obtained in Section 2 and the results by the continuous Boltzmann simulation in Section 3 are shown in the same figure. The agreement with the continuous Boltzmann equation is perfect. They approach the no-slip Navier-Stokes solution as expected as τ or the Knudsen number Kn decreases.
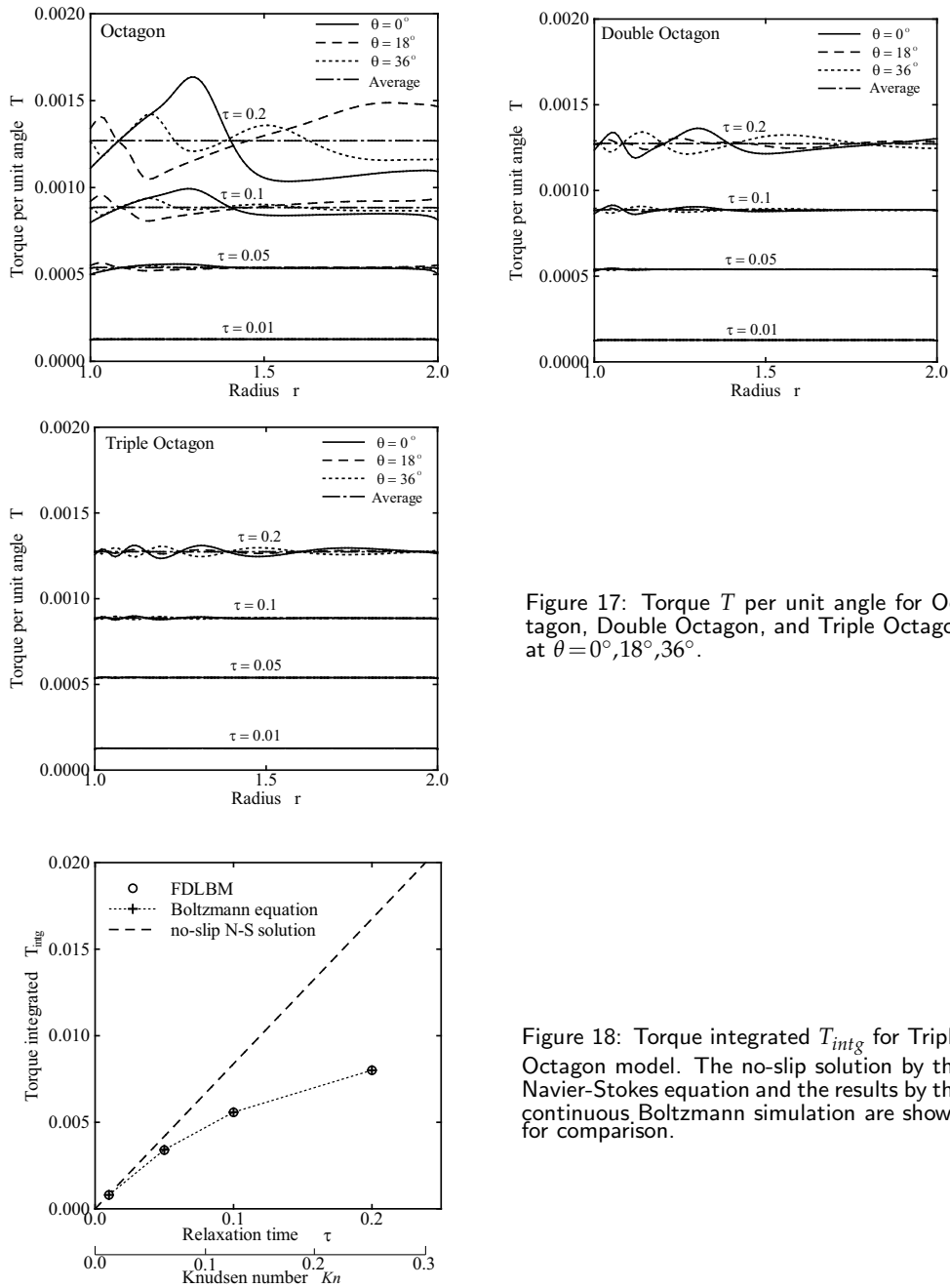
Figure 17: Torque T per unit angle for Octagon, Double Octagon, and Triple Octagon at $\theta = 0°, 18°, 36°$.

Figure 18: Torque integrated T_{intg} for Triple Octagon model. The no-slip solution by the Navier-Stokes equation and the results by the continuous Boltzmann simulation are shown for comparison.

5.2 Results by the D2Q9 model

The rotational velocity u_θ in the flow domain for the D2Q9 model with various τ are shown in Fig. 19.
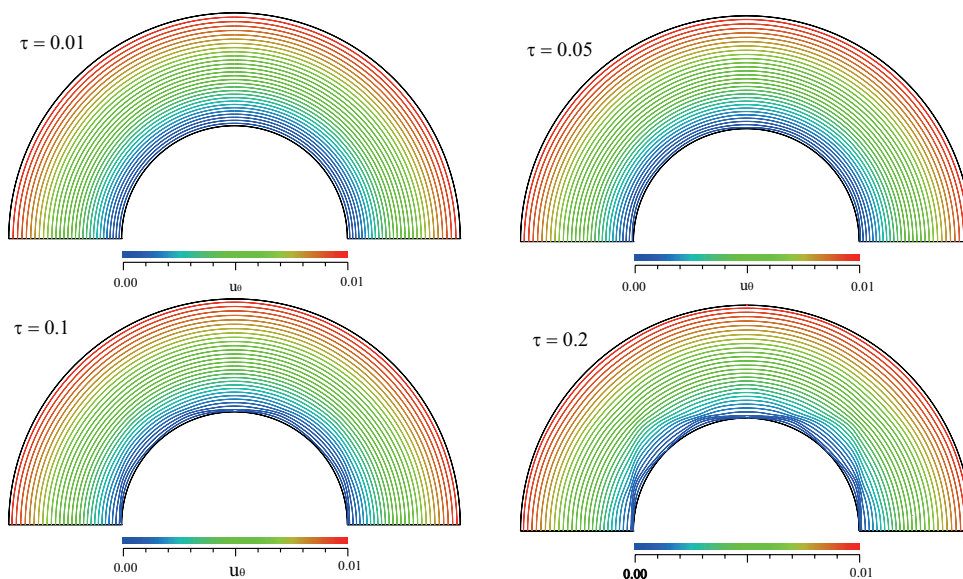
Figure 19: D2Q9 model. Rotational velocity u_θ in the flow domain for $\tau = 0.01, 0.05, 0.1$ and 0.2.
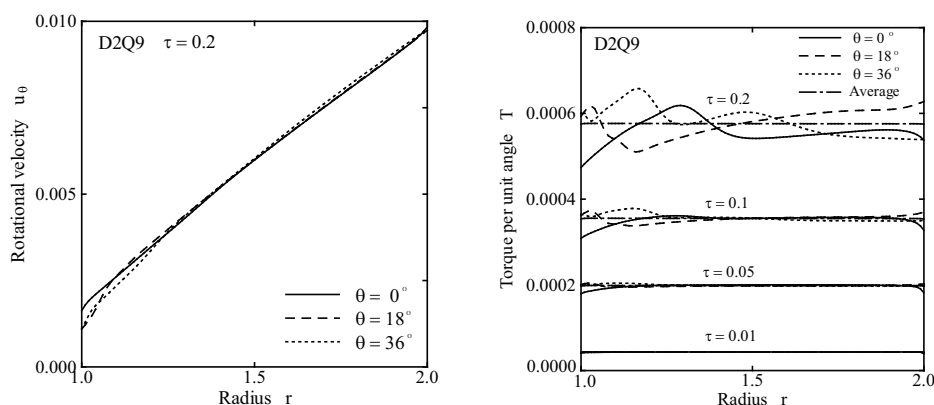
Figure 20: D2Q9 model. Rotational velocity u_θ for $\tau = 0.2$ and torque T per unit angle for various τ at $\theta = 0°, 18°, 36°$.

The rotational velocity u_θ for $\tau = 0.2$ and the torque T per unit angle at the angles $\theta = 0°, 18°, 36°$ are shown in Fig. 20. The non-uniformity due to the angle θ is as large as the Octagon model.

5.3 Computing time

Simulations were performed using a personal Dell Inspiron 1525 computer with Intel Core2. The computing time required to obtain a steady state for the continuous Boltzmann and the FDLBM simulations with $\tau = 0.01$ and 0.1 are summarized in Table 3. In the

Table 3: Computing time required to obtain a steady state for the continuous Boltzmann and the FDLBM simulations with $\tau = 0.01$ and 0.1.

	Cont. Boltz.	Triple Oct.	Double Oct.	Octagon	D2Q7
$\tau = 0.01$	14288min	582min	391min	217min	99min
	(9d 22h 8min)	(9h 42min)	(6h 31min)	(3h 37min)	(1h 39min)
$\tau = 0.1$	2312min	88min	61min	31min	13min
	(38h 32min)	(1h 28min)	(1h 1min)		
Velocity space	501×200	$1+4 \times 24$	$1+4 \times 16$	$1+4 \times 8$	$1+8$
Physical space	101	101×105	101×105	101×105	101×105

table, the grid size of the velocity space or the number of velocity particles, and the grid size of the physical space are also summarized. The computing time for $\tau = 0.01$ is about 7 times that for $\tau = 0.1$ since transmission of the torque is slow from the low viscosity. The ratio of computing time for the Triple Octagon, Double Octagon, Octagon, and D2Q9 is roughly $6:4:2:1$. It is understandable that the computing time for the FDLBM simulation increases in proportion to the number of velocity particles since the physical spaces are common. The computing time for the continuous Boltzmann simulation is about 25 times that for the Triple Octagon simulation. If the continuous Boltzmann simulation were to be performed with the same physical space grids, the computing time would be 2500 times that for the Triple Octagon simulation. If a more efficient integration method is applied to the continuous Boltzmann simulation or the accuracy is compromised, it is possible to apply a coarser grid system and to shorten the computing time. Nevertheless, directly solving the continuous Boltzmann equation remains a daunting task.

6   Conclusions

Numerical simulations of rotational slip flow in coaxial cylinders were conducted to study applicability of the LBM and FDLBM to a velocity slip phenomenon in 2D environment. The cylindrical coordinate system was successfully applied.

In order to decrease the dependency on the inclination angle to the wall, sufficient number of directions of velocity particles are necessary. The Octagon and D2Q9 models, whose moving velocity particles go forward in eight directions, show a strong dependency on the inclination angle when the Knudsen number is large. The dependency on the inclination angle for the Triple Octagon model whose moving velocity particles go forward in 24 directions is quite small. The simulation results by the Triple Octagon model agree very well with those by the continuous Boltzmann simulation and approaches the no-slip Navier-Stokes solution as the limit of small Knudsen number.

An increase in accuracy is accomplished in compensation for the computational cost. The ratio of computing time for the Triple Octagon, Double Octagon, Octagon, and D2Q9 is roughly $6:4:2:1$, which is proportional to the number of velocity particles. If the continuous Boltzmann simulation were to be performed with the same physical space

grids as the FDLBM, the computing time would be 2500 times that for the Triple Octagon simulation. Even if a more efficient integration method is applied or the accuracy is compromised, directly solving the continuous Boltzmann equation remains a daunting task.

The author believes that the FDLBM is an ideal solver in an intermediate flow, where both the Navier-Stokes flow and the rarefied flow co-exist, if the model has sufficient velocity particles like the Triple Octagon model.

Appendix

Boltzmann equation in the cylindrical coordinate system

The Boltzmann equation in the cylindrical coordinate system is summarized [15,16]. The convection term of the Boltzmann equation in the Cartesian coordinate, where the independent variables are (x,y,c_x,c_y), is expressed as

$$c_x\frac{\partial f}{\partial x}+c_y\frac{\partial f}{\partial y}. \tag{A.1}$$

If the cylindrical coordinate system (r,θ) is introduced to the physical space, several expressions for the convection term are possible depending on the treatment of the velocity space (c_1,c_2) (see Fig. 21). The spatial derivatives are changed according to the following relations:

$$\frac{\partial}{\partial x}=\frac{\partial r}{\partial x}\frac{\partial}{\partial r}+\frac{\partial\theta}{\partial x}\frac{\partial}{\partial\theta}+\frac{\partial c_1}{\partial x}\frac{\partial}{\partial c_1}+\frac{\partial c_2}{\partial x}\frac{\partial}{\partial c_2}, \tag{A.2}$$

$$\frac{\partial}{\partial y}=\frac{\partial r}{\partial y}\frac{\partial}{\partial r}+\frac{\partial\theta}{\partial y}\frac{\partial}{\partial\theta}+\frac{\partial c_1}{\partial y}\frac{\partial}{\partial c_1}+\frac{\partial c_2}{\partial y}\frac{\partial}{\partial c_2}. \tag{A.3}$$

The relationship between (x,y) and (r,θ) is

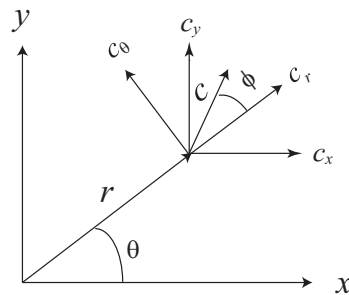$$r=\sqrt{x^2+y^2}, \qquad \theta=\tan^{-1}\left(\frac{y}{x}\right). \tag{A.4}$$

Figure 21: Cylindrical coordinate system: the physical space and velocity space.

Consequently,

$$\frac{\partial r}{\partial x} = \cos\theta, \quad \frac{\partial r}{\partial y} = \sin\theta, \quad \frac{\partial \theta}{\partial x} = -\frac{\sin\theta}{r}, \quad \frac{\partial \theta}{\partial y} = \frac{\cos\theta}{r}. \tag{A.5}$$

Cylindrical coordinate 1: $f(r,\theta,c_x,c_y)$

This expression was adopted in the FDLBM simulation. The velocity space remains unchanged; consequently, is independent from the physical space

$$\frac{\partial c_x}{\partial x} = \frac{\partial c_x}{\partial y} = \frac{\partial c_y}{\partial x} = \frac{\partial c_y}{\partial y} = 0. \tag{A.6}$$

Therefore, the convection term is expressed as

$$(c_x\cos\theta + c_y\sin\theta)\frac{\partial f}{\partial r} + \frac{-c_x\sin\theta + c_y\cos\theta}{r}\frac{\partial f}{\partial \theta}. \tag{A.7}$$

Cylindrical coordinate 2: $f(r,\theta,c,\phi)$

This expression was adopted in the continuous Boltzmann simulation. The velocity space rotates in accordance with the physical space. The variables (c,ϕ) are expressed as

$$c = \sqrt{c_x^2 + c_y^2}, \quad \phi = \tan^{-1}\left(\frac{-c_x y + c_y x}{c_x x + c_y y}\right), \tag{A.8}$$

$$\frac{\partial c}{\partial x} = \frac{\partial c}{\partial y} = 0, \quad \frac{\partial \phi}{\partial x} = \frac{\sin\theta}{r}, \quad \frac{\partial \phi}{\partial y} = -\frac{\cos\theta}{r}. \tag{A.9}$$

Consequently, the convection term becomes

$$
\begin{aligned}
&(c_x\cos\theta + c_y\sin\theta)\frac{\partial f}{\partial r} + \frac{-c_x\sin\theta + c_y\cos\theta}{r}\frac{\partial f}{\partial \theta} + \frac{c_x\sin\theta - c_y\cos\theta}{r}\frac{\partial f}{\partial \phi} \\
&= (c_x\cos\theta + c_y\sin\theta)\frac{\partial f}{\partial r} + \frac{-c_x\sin\theta + c_y\cos\theta}{r}\left(\frac{\partial f}{\partial \theta} - \frac{\partial f}{\partial \theta}\right) \\
&= c\cos\phi\frac{\partial f}{\partial r} + \frac{c\sin\phi}{r}\left(\frac{\partial f}{\partial \theta} - \frac{\partial f}{\partial \phi}\right).
\end{aligned}
\tag{A.10}
$$

Cylindrical coordinate 3: $f(r,\theta,c_r,c_\theta)$

This expression frequently appears in texts. The velocity space rotates in accordance with the physical space and the variables (c_r,c_θ) are functions of (x,y),

$$c_r = \frac{c_x x + c_y y}{\sqrt{x^2 + y^2}}, \quad c_\theta = \frac{-c_x y + c_y x}{\sqrt{x^2 + y^2}}, \tag{A.11}$$

$$\frac{\partial c_r}{\partial x} = -\frac{c_\theta \sin\theta}{r}, \quad \frac{\partial c_r}{\partial y} = \frac{c_\theta \cos\theta}{r}, \quad \frac{\partial c_\theta}{\partial x} = \frac{c_r \sin\theta}{r}, \quad \frac{\partial c_\theta}{\partial y} = -\frac{c_r \cos\theta}{r}. \tag{A.12}$$

Consequently, the convection term becomes

$$
(c_x\cos\theta + c_y\sin\theta)\frac{\partial f}{\partial r} + \frac{-c_x\sin\theta + c_y\cos\theta}{r}\frac{\partial f}{\partial \theta} + \frac{c_\theta(-c_x\sin\theta + c_y\cos\theta)}{r}\frac{\partial f}{\partial c_r}
$$
$$
+ \frac{c_r(c_x\sin\theta - c_y\cos\theta)}{r}\frac{\partial f}{\partial c_\theta} = c_r\frac{\partial f}{\partial r} + \frac{c_\theta}{r}\frac{\partial f}{\partial \theta} + \frac{c_\theta^2}{r}\frac{\partial f}{\partial c_r} - \frac{c_r c_\theta}{r}\frac{\partial f}{\partial c_\theta}. \tag{A.13}
$$

References

[1] C. Y. Lim, C. Shu, X. D. Niu, and Y. T. Chew, Application of lattice Boltzmann method to simulate microchannel flows, Phys. Fluids., 14 (2002), 2299–2308.

[2] X. Nie, G. D. Doolen, and S. Chen, Lattice-Boltzmann simulations of fluid flows in MEMS, J. Stat. Phys. 107 (2002), 279–289.

[3] M. Sbragaglia, and S. Succi, Analytical calculation of slip flow in lattice Boltzmann models with kinetic boundary conditions, Phys. Fluids., 17 (2005), 093602.

[4] S. Ansumali, and I. V. Karlin, Kinetic boundary conditions in the lattice Boltzmann method, Phys. Rev. E., 66 (2002), 026311.

[5] G. H. Tang, W. Q. Tao, and Y. L. He, Lattice Boltzmann method for gaseous microflows using kinetic theory boundary conditions, Phys. Fluids., 17 (2005), 058101.

[6] Y. Zhang, R. Qin, and D. R. Emerson, Lattice Boltzmann simulation of rarefied gas flows in microchannels, Phys. Rev. E., 71 (2005), 047702.

[7] X. D. Niu, S. A. Hyodo, T. Munekata, and K. Suga, Kinetic lattice Boltzmann method for microscale gas flows: issues on boundary condition, relaxation time, and regularization, Phys. Rev. E., 76 (2007), 036711.

[8] V. Sofonea, and R. F. Sekerka, Diffuse-reflection boundary conditions for a thermal lattice Boltzmann model in two dimensions: evidence of temperature jump and slip velocity in microchannels, Phys. Rev. E., 71 (2005), 066709.

[9] V. Sofonea, and R. F. Sekerka, Boundary conditions for the upwind finite difference lattice Boltzmann model: evidence of slip velocity in micro-channel flow, J. Comput. Phys., 207 (2005), 639–659.

[10] M. Watari, Velocity slip and temperature jump simulations by the three-dimensional thermal finite-difference lattice Boltzmann method, Phys. Rev. E., 79 (2009), 066706.

[11] M. Watari, Relationship between accuracy and number of velocity particles of the finite-difference lattice Boltzmann method in velocity slip simulations, J. Fluids. Eng., 132 (2010), 101401.

[12] M. Watari, and M. Tsutahara, Two-dimensional thermal model of the finite-difference lattice Boltzmann method with high spatial isotropy, Phys. Rev. E., 67 (2003), 036306.

[13] Y. H. Qian, D. D'Humieres, and P. Lallemand, Lattice BGK models for Navier-Stokes equation, Europhys. Lett., 17 (1992), 479–484.

[14] R. A. Millikan, Coefficients of slip in gases and the law of reflection of molecules from the surfaces of solids and liquids, Phys. Rev., 21 (1923), 217–238.

[15] M. N. Kogan, Rarefied Gas Dynamics, Plenum, New York, 1969.

[16] Y. Sone, Molecular Gas Dynamics: Theory, Techniques, and Applications, Birkhäuser, Boston, 2006.